Journal of Magnetic Resonance 200 (2009) 178–188

Contents lists available at ScienceDirect

Journal of Magnetic Resonance

journal homepage: www.elsevier.com/locate/jmr

Double-quantum NMR spectroscopy of ^{31}P species submitted to very large CSAs

B. Hu, L. Delevoye, O. Lafon, J. Trébosc, J.P. Amoureux *

UCCS, CNRS-8181, Lille-University, Villeneuve D'Ascq, France

ARTICLE INFO

Article history:
Received 20 May 2009
Revised 24 June 2009
Available online 30 June 2009

Keywords:
Solid-state NMR
Double-quanta
Large CSA
Phosphorous atoms

ABSTRACT

We introduce an original pulse sequence, $BR2^1_2(\tau\pi\tau)$, which is a block super-cycled $R2^1_2$ sequence employing as basic element a π pulse sandwiched by 'window' intervals. This homonuclear dipolar recoupling method allows the efficient excitation of double-quantum coherences between spin-1/2 nuclei submitted to very large chemical shift anisotropy. We demonstrate that this technique can be employed in double-quantum ↔ single-quantum ^{31}P homonuclear correlation experiment at high magnetic field ($B_0 \geqslant 14$ T) and high MAS frequencies ($\nu_R \geqslant 30$ kHz). The performances of $BR2^1_2(\tau\pi\tau)$ are compared to those of the double-quantum recoupling methods, such as BABA and bracketed fp-RFDR, which were already employed at fast MAS rates. The $BR2^1_2(\tau\pi\tau)$ sequence displays a higher robustness to CSA and offset than the other existing techniques.

1. Introduction

Solid-state ^{31}P nuclear magnetic resonance (NMR) benefits from the favorable nuclear properties of this spin-1/2 isotope, characterized by a high gyromagnetic ratio ($\gamma_{31P} = 0.40\gamma_{1H} = 1.61\gamma_{13C}$) and a 100% natural isotopic abundance. Furthermore, the ^{31}P isotropic chemical shifts (δ_{iso}) cover nearly 2000 ppm, allowing a clear distinction between various local environments of phosphorous atoms [1]. In solids and mesophases, the chemical shift anisotropy (CSA), which is in the order of 100–200 ppm, provides additional information on the symmetry of the ^{31}P sites [2]. Owing to these advantageous properties, solid-state ^{31}P NMR spectroscopy has been employed to characterize biological molecules [3,4], such as proteins in the phosphorylated state, phospholipids and nucleic acids, as well as inorganic materials, such as phosphate glasses and porous aluminophosphates [4].

Two-dimensional (2D) ^{31}P homonuclear correlation (HOMCOR) experiments have been introduced in order to probe the connectivity and the proximity of the different ^{31}P sites in solids. Coherence transfers between nearby ^{31}P nuclei can be achieved via the *J*-couplings (*J*-HOMCOR) [5,6] or the dipole–dipole (DD) couplings (*D*-HOMCOR) [7–13]. *J*-HOMCOR and *D*-HOMCOR methods are complementary, since *J*-HOMCOR reveals the through-bond connectivity while *D*-HOMCOR provides information on the through-space proximity. The 2D HOMCOR experiments can select either single- (1Q), double- (2Q) or multiple-quantum (MQ) coherences during the t_1 period [14]. Compared to 1Q–1Q correlation experiments, the 2Q–1Q and MQ–1Q correlation spectroscopies benefit from the possibility to probe correlation between equivalent sites. The focus here is on 2Q–1Q ^{31}P *D*-HOMCOR [7–13].

D-HOMCOR on polycrystalline and disordered materials employs a combination of two methods: (i) magic-angle spinning (MAS) for improving spectral resolution and sensitivity and (ii) homonuclear recoupling techniques [8,10,15–38], to reintroduce selectively the dipolar couplings, which are averaged out by MAS. Two classes of homonuclear recoupling techniques can be employed in order to excite the double-quantum coherences (2QCs) in 2Q–1Q *D*-HOMCOR experiment. We can use either direct 2Q-recoupling sequences, such as BABA [8,22] and POST-C7 [24], or 0Q-recoupling schemes, such as finite-pulse RFDR (fp-RFDR) [32], bracketed by a pair of $\pi/2$-pulses: [fp-RFDR] [33,37,40]. In the case of ^{31}P nuclei, homonuclear 2QCs have been created under MAS condition by using BABA [8], [fp-RFDR] [12], and RN^{ν}_{n} or CN^{ν}_{n} symmetry-based sequences [9–11,13], such as POST-C7 [24]. These recoupling methods allow to obtain 2D 2Q–1Q *D*-HOMCOR experiments and to estimate the ^{31}P–^{31}P inter-nuclear distances [11,41,42].

Up to now, ^{31}P recoupling schemes were mainly applied at moderate static magnetic fields ($B_0 \leqslant 11.7$ T). Higher magnetic fields can lead in principle to substantial benefits in terms of sensitivity and resolution. However, the magnitude of the CSA, in Hz, is proportional to B_0. As a result, ^{31}P nuclei in phosphate groups can experience CSAs as large as 81 kHz at 23.5 T (the largest magnetic field presently commercially available), when $\delta_{aniso} = 200$ ppm. In that case, the magnitude of ^{31}P CSA is comparable with that of the radio-frequency (rf) fields and is much larger than the ^{31}P–^{31}P dipolar interactions, which do not exceed 1.8 kHz in magnitude [4]. Therefore, large ^{31}P CSAs can interfere with the homonuclear recoupling sequences and they may decrease the excitation efficiency of 2QCs [11]. The robustness of the recoupling sequences to resonance off-

* Corresponding author. Address: UCCS UMR 8181 au CNRS, Universite de Lille I, FR-59655 Villeneuve D'Ascq Cedex, France. Fax: +33 3 20 43 68 14.
E-mail address: jean-paul.amoureux@univ-lille1.fr (J.P. Amoureux).

1090-7807/$ - see front matter © 2009 Elsevier Inc. All rights reserved.
doi:10.1016/j.jmr.2009.06.020

set is generally less critical, since in most of phosphorous-containing samples, such as phosphate glasses, the phosphorous atoms occupy similar sites and the offset range is limited to about 20 ppm, i.e., 8.1 kHz at 23.5 T in these compounds.

The interference of ^{31}P CSA with dipolar recoupling sequences at high magnetic fields can only be circumvented by combining: (i) a high MAS frequency ($\nu_R \geqslant 30$ kHz) and (ii) dipolar recoupling sequences that suppress the CSA internally. Only a few existing dipolar recoupling schemes meet both requisites. The BABA sequences can be employed at high MAS rates but are sensitive to CSA [8]. Even the use of a super-cycle spanning four rotor periods does not permit a total elimination of the CSA during BABA recoupling schemes. The symmetry-based sequences allow for a better compensation of CSA, but most of them cannot be employed at high MAS frequencies owing to the need for large rf fields. For instance, POST-C7 requires the nutation frequency to be seven times the sample spinning frequency. Such high rf power for extended time periods of tens of ms is not compatible with probe rf-limitations and can lead to the unwanted heating of high water and salt content samples, such as bio-molecules. The symmetry-based sequences with lower rf field requirements are more promising for fast MAS solid-state NMR. Recently, we demonstrated that a sequence derived from the $R2_2^1$ symmetry achieved an efficient ^{1}H–^{1}H 2Q dipolar recoupling at high spinning speeds [39]. This sequence denoted SPIP (Sandwiched PI Pulse) was also shown to be robust to offset for ^{1}H spectra.

The purpose of the present contribution is to develop 2Q–1Q ^{31}P *D*-HOMCOR experiments at high magnetic fields ($B_0 \geqslant 14.0$ T) and high MAS frequencies ($\nu_R \geqslant 30$ kHz). We compare the performances of different ^{31}P dipolar recoupling methods, such as BABA, [fp-RFDR] and SPIP. We also propose a new pulse sequence, $BR2_2^1(\tau\pi\tau)$, based on the $R2_2^1$ sequence [14,37,43], which does not need large rf power. The experiments were performed on large field spectrometers (up to 18.8 T in this work), with fast (30 kHz for the experiments) or ultra-fast (up to 65 kHz in the simulations) spinning speeds. The analysis has been performed on systems with ^{31}P dipolar-coupling 3D networks, and not only on isolated ^{31}P–^{31}P spin pairs.

2. Pulse sequences

2.1. 1D 2QF and 2D 2Q–1Q *D*-HOMCOR experiments

The general scheme of 2Q–1Q *D*-HOMCOR experiments is described in Fig. 1a. A first recoupling sequence is applied for an interval τ_{exc} in order to transform the longitudinal magnetization into 2QCs. A second recoupling period of duration τ_{rec}, followed by a $\pi/2$ pulse, transforms the 2QCs into observable transverse magnetization. Signals passing through 2QCs are selected by a four-step phase cycle of the pulses used for exciting or reconverting the 2QCs. For 1D 2Q-filtered (2QF) sequences, there is no evolution period, $t_1 = 0$, whereas for 2D 2Q–1Q *D*-HOMCOR experiments, the t_1 delay is incremented. Hence, the evolution of 2QCs during t_1 is correlated with that of 1Q-coherences during t_2 and the resulting 2D spectra display 2Q–1Q correlations. Different homonuclear dipolar recoupling sequences can be applied during τ_{exc} and τ_{rec} periods. We employ symmetry-based recoupling sequences, such as BABA, SPIP, $BR2_2^1(\tau\pi\tau)$ and [fp-RFDR]. The robustness of these sequences to ^{31}P CSA is improved by super-cycling, i.e., repetition of the pulse sequence with an additional overall phase shift and/or a change in sign of all phases [8,34,36,38,44]. These super-cycles may sacrifice the favorable properties of 'γ-encoding' for the sake of greater robustness [34]. All the super-cycled recoupling sequences employed in this article are non-γ-encoded, and hence the evolution time t_1 must be an integer multiple of rotor periods, which limits the F_1 spectral width.

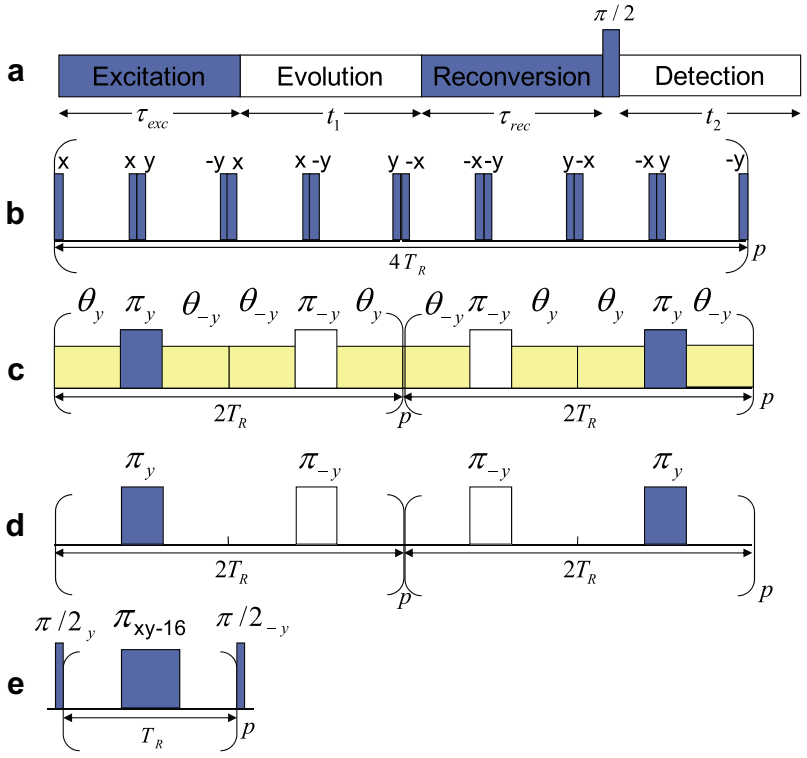

Fig. 1. (a) General scheme of 2Q–1Q spectroscopy. Basic cycle of: (b) BABA-4, (c) SPIP, (d) $BR2_2^1(\tau\pi\tau)$, (e) [fp-RFDR]. The XY-16 super-cycle consists in (x, y, x, y), (y, x, y, x), $(-x, -y, -x, -y)$ and $(-y, -x, -y, -x)$ [49]. The pulse sequence in Fig. 2 of Ref. [12] was mistyped. It actually has one π pulse per rotor period, and is identical with that shown in (e).

2.2. Average Hamiltonian theory

The properties of the investigated symmetry-based recoupling sequences can be analyzed by using both the average Hamiltonian theory (AHT) and symmetry arguments [34,44]. The effective Hamiltonian, $\overline{H}$, describing the synchronous evolution of the spin system, can be expanded in terms of increasing order of perturbation by using the Magnus expansion [34,45]:

$$\overline{H} = \overline{H}^{(1)} + \overline{H}^{(2)} + \cdots \tag{1}$$

where the upper indices give the order of perturbation. If the internal spin interactions expressed in Hz are smaller than the inverse period of the pulse sequence, the Magnus expansion converges after the first or second term. This convergence criteria may not hold for ^{31}P nuclei in large B_0 field since the CSA can be larger than the MAS frequency, whereas the period of rotor-synchronized pulse sequences is always larger than or equal to the rotor period $T_R = 1/\nu_R$. Even if terminating the Magnus expansion after the first and second-order terms is a crude approximation in the case of ^{31}P NMR experiments, we show below that these first two terms provide some physical insights into the spin dynamics during the recoupling sequences. In particular, $\overline{H}^{(1)}$ and $\overline{H}^{(2)}$ Hamiltonians allow a qualitative prediction of the dependences of efficiency and optimal recoupling time with the pulse length (see Figs. 2 and 4). Therefore, the AHT of the investigated symmetry-based recoupling sequences is briefly discussed below. The general theory of symmetry-based recoupling sequences may be found in Refs. [34,43,44].

The terms in the Magnus expansion subsume the contributions of the different spin interactions. In general, the higher the order the lower the magnitude. Each interaction Λ is characterized by its transformation properties under rotations of the molecular framework and the nuclear magnetic moments. The space and spin rotational properties are specified by the space rank l and the spin rank λ, respectively. The various nuclear spin interactions are distinguished by the values of l and λ. For instance, the pair $\{l, \lambda\}$ is equal to {2, 2} for homonuclear DD interaction, {2, 1} for CSA, {0, 1} for δ_{iso}. Each spin interaction may be regarded as a superposition of $(2l + 1) \times (2\lambda + 1)$ components, with component indexes m and μ running, respectively, from $-l$ to $+l$, and $-\lambda$ to $+\lambda$ in integer steps. Therefore, each term in the expansion of Eq. (1) is the sum of many different components:

$$\overline{H}^{(1)} = \sum_{\mathbf{1}} \overline{H}^{(1)}_{\mathbf{1}} \tag{2}$$

$$\overline{H}^{(2)} = \sum_{\mathbf{2}} \sum_{\mathbf{1}} \overline{H}^{(2)}_{\{\mathbf{1},\mathbf{2}\}} \tag{3}$$

where the bold index **1** is used to represent the term of interaction Λ_1 with quantum numbers $\{l_1, m_1, \lambda_1, \mu_1\}$ and similarly for **2**. The sum of Eq. (2) is taken over all spin interactions of the system and all combinations of quantum numbers, whereas the sum of Eq. (3) is taken over all cross-terms between a term of interaction Λ_1 with quantum numbers $\{l_1, m_1, \lambda_1, \mu_1\}$ and that of interaction Λ_2 with quantum numbers $\{l_2, m_2, \lambda_2, \mu_2\}$. The symmetry properties and the super-cycle of 2Q homonuclear recoupling sequences must be such that some homonuclear DD coupling 2Q terms with $\mu = \pm 2$ are symmetry-allowed in $\overline{H}^{(1)}$, and all CSA and δ_{iso} terms are symmetry-forbidden to first-order. The optimal length of τ_{exc} and τ_{rec} delays in 2Q–1Q D-HOMCOR experiments depends on the amplitude of the recoupled 2Q DD interaction. This amplitude depends on the recoupling sequence through the set of scaling factors $\kappa_{lm\lambda\mu}$ where $\{l, m, \lambda, \mu\} = \{2, m, 2, \pm 2\}$ and $m = \pm 1, \pm 2$ are all symmetry-allowed quantum numbers characterizing the 2Q DD interaction. A qualitative factor subsuming the strength of the recoupled 2Q DD interaction may be assessed by taking the root mean square (rms) of the symmetry-allowed scaling factors [46]:

$$\kappa^{rms}_{DD2Q} = \left(\sum_m \left[|\kappa_{2m22}|^2 + |\kappa_{2m2-2}|^2 \right] \right)^{1/2} \tag{4}$$

where the sum is taken over $m = \pm 1, \pm 2$. It must be reminded here that this κ^{rms}_{DD2Q} factor is roughly proportional to the 2QC build-up rate, i.e., proportional to the inverse of the optimal recoupling time. It does not affect directly the maximal efficiency. The analytical expressions of $\kappa_{lm\lambda\mu}$ for CN^{ν}_{n} and RN^{ν}_{n} sequence are given in Ref. [43]. The $\kappa_{lm\lambda\mu}$ values were calculated by using the 'C and R symmetries' Mathematica package which takes into account the super-cycle [30,43,47,48,26]. Note that owing to the insertion of bracketing $\pi/2$-pulses, the [fp-RDFR] sequence does not belong to CN^{ν}_{n} and RN^{ν}_{n} symmetry classes, and its κ^{rms}_{DD2Q} value cannot be directly calculated with this package. However, fp-RDFR is a 0Q recoupling scheme, which originates from $R4^1_4$ symmetry. The bracketing $\pi/2$-pulses

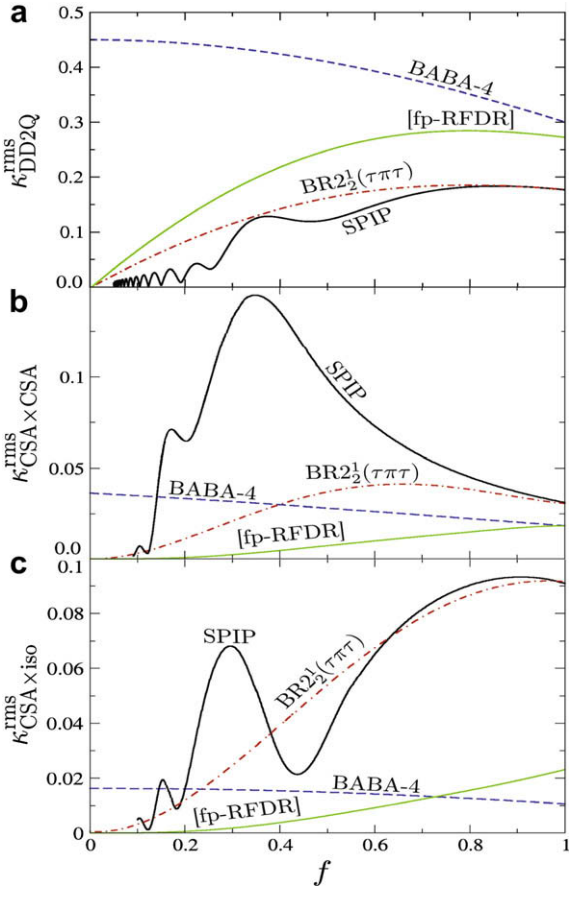

Fig. 2. Simulations of first- and second-order rms scaling factors plotted as function of the pulse fraction f, as defined in Eq. (7), for BABA, SPIP, BR2$^1_2(\tau\pi\tau)$ and [fp-RFDR] recoupling methods. The 'C and R symmetries' Mathematica package has been used and the super-cyclings have been taken into account [30,43,47,48,26]. Curve (a) displays the rms scaling factor, κ^{rms}_{DD2Q}, defined in Eqs. (4) and (5), of the desired DD coupling 2Q terms, while curves (b) and (c) display the rms scaling factors, $\kappa^{rms}_{CSA\times CSA}$ and $\kappa^{rms}_{CSA\times iso}$, defined in Eq. (6), of unwanted second-order cross-terms. The $\kappa^{rms}_{CSA\times CSA}$ and $\kappa^{rms}_{CSA\times iso}$ values allow a qualitative assessment of the CSA and offset interferences. These curves were calculated for BABA, SPIP, BR2$^1_2(\tau\pi\tau)$ sequences spanning 4 rotor periods and [fp-RFDR] sequence with XY-16 super-cycle spanning 16 rotor periods. Thus, the SPIP and BR2$^1_2(\tau\pi\tau)$ sequences correspond to $(R2^1_2)^1(R2^{-1}_2)^1$ symmetry. For the SPIP method, the rf nutation frequency of the bracketing θ pulses is fixed to 70% of that of π pulses, i.e., $\nu_{1\theta} = 0.7\nu_{1\pi}$. Note that if this figure properly predicts the dependence of the optimal efficiency and recoupling time with the f value, it fails in explaining why SPIP sequence with $f > 0.2$ ($\nu_1 < 2.5\nu_R$) is more robust to CSA and offset than BABA sequences. This discrepancy clearly evidences the limitations of the AHT up to the second order, when the ^{31}P CSA is larger than the spinning speed. In that case, only numerically exact simulations allow a quantitative assessment of CSA interferences.

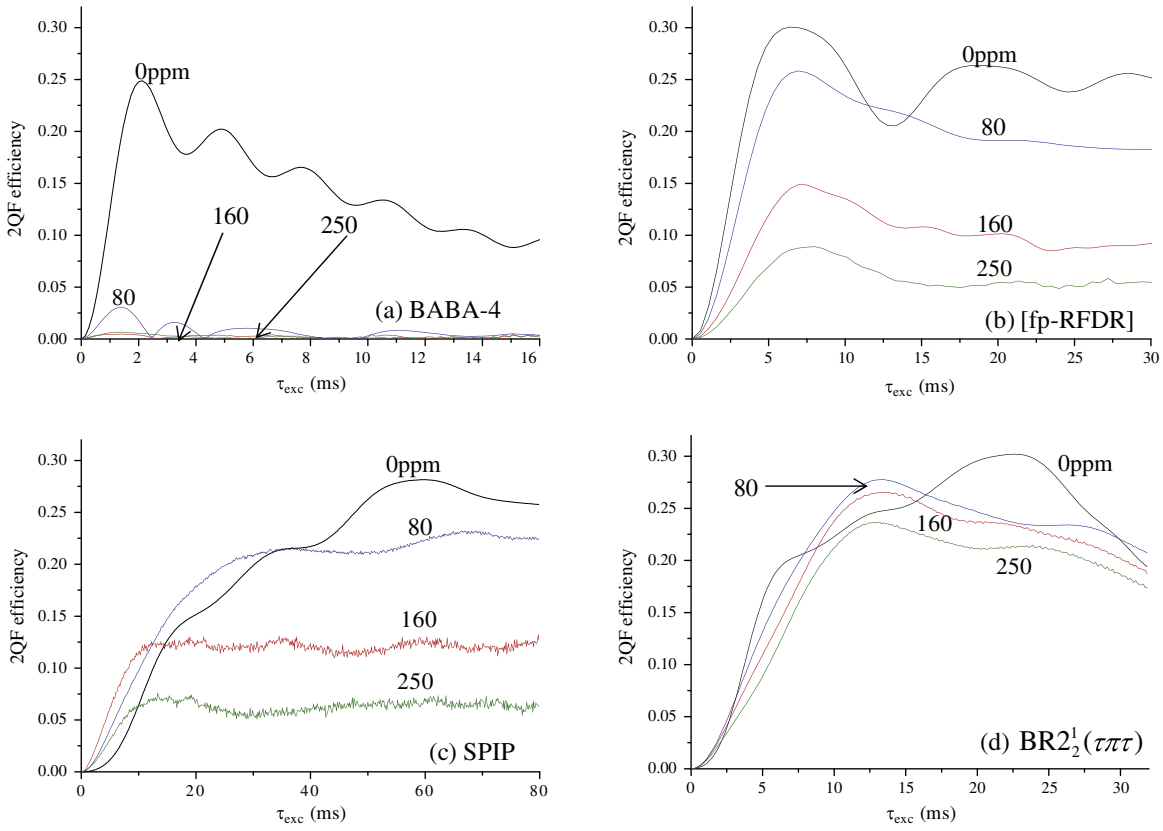

Fig. 3. Simulations of ^{31}P 1D 2QF build-up curves of one ^{31}P–^{31}P spin pair with $b/(2\pi) = -263$ Hz. Both nuclei were submitted to two identical CSAs, with asymmetry parameter $\eta = 0.1$. The simulations were performed for four different recoupling sequences at $B_0 = 18.8$ T and $\nu_R = 30$ kHz. Four different δ_{aniso} values were employed: 0, 80, 160 or 250 ppm. The δ_{aniso} value corresponding to each plot is indicated in the figure. The rf irradiation was applied in the middle of these two resonances, which are separated by a difference in isotropic chemical shift of $\Delta\delta_{iso} = 2$ ppm. For each pulse sequence, the pulse fraction f was optimized: (a) BABA-4 with $f = 0.3$ (b) [fp-RFDR] with $f = 0.33$, (c) SPIP with $f = 0.167$, (d) BR2$^1_2(\tau\pi\tau)$ with $f = 0.167$. The bracketing $\pi/2$ pulses are ideal pulses.

only convert a part of the DD coupling 0Q terms into 2Q terms. Therefore, the scaling factor of 2Q terms for [fp-RFDR] can be calculated from that of 0Q terms reintroduced by fp-RFDR, according to

$$\kappa^{rms}_{DD2Q}([\text{fp-RFDR}]) = \frac{\sqrt{3}}{2}\kappa^{rms}_{DD0Q}(\text{fp-RFDR}) = \frac{\sqrt{3}}{2}\left(\sum_m |\kappa_{2m20}(\text{fp-RFDR})|^2\right)^{1/2} \quad (5)$$

The above expression is demonstrated in Appendix A. If the symmetry properties of BABA, SPIP, BR2$^1_2(\tau\pi\tau)$ and [fp-RFDR] restore selectively the ^{31}P–^{31}P DD interactions to first-order, the CSA and resonance offsets are much larger than the DD interactions in the case of ^{31}P nuclei. Hence, a first-order analysis is often insufficient. As pointed out above, the CSA of ^{31}P nuclei in large B_0 field is usually larger than the inverse period of the pulse sequence. Therefore, the CSA and δ_{iso} interferences are not limited to the second-order terms but can involve higher order terms. Nevertheless, in this article, the AHT treatment is confined to the first and second order terms. The influence of higher order terms will only be evidenced by comparison between AHT predictions and numerically exact simulations. The second-order Hamiltonian allows qualitative assessment of CSA and δ_{iso} interferences. For ^{31}P recoupling, the $\bar{H}^{(2)}$ Hamiltonian is generally dominated by CSA × CSA and CSA × δ_{iso} cross-terms. The size of these undesirable terms may be assessed by calculating the rms scaling factor of CSA × CSA and CSA × δ_{iso} cross-terms, $\kappa^{rms}_{CSA\times CSA}$ and $\kappa^{rms}_{CSA\times iso}$. These second-order scaling factors are given by

$$\kappa^{rms}_{\Lambda_1\times\Lambda_2} = \left(\sum_{\{\mathbf{1},\mathbf{2}\}} |\kappa_{\{\mathbf{1},\mathbf{2}\}}|^2\right)^{1/2} \quad (6)$$

where the sum is taken over all symmetry-allowed cross-terms, {**1**, **2**}, between a term of interaction Λ_2 with quantum number {l_2, m_2, λ_2, μ_2} and that of interaction Λ_1 with quantum number {l_1, m_1, λ_1, μ_1}. The second-order scaling factor, $\kappa_{\{\mathbf{1},\mathbf{2}\}}$, can be evaluated from the analytical forms given in Ref. [44] and their implementation in the 'C and R symmetries' package. The scaling factors of BABA, SPIP, BR2$^1_2(\tau\pi\tau)$ and [fp-RFDR] depend on the relative durations between the pulses and the windows, i.e., the pulse fraction f

$$f = \begin{cases} 4\tau_{\pi/2}/T_R & \text{for BABA} \\ \tau_\pi/T_R & \text{for SPIP, BR2}^1_2(\tau\pi\tau), \text{[fp-RFDR]} \end{cases} \quad (7)$$

Fig. 2 compares the dependences of scaling factors, κ^{rms}_{DD2Q}, $\kappa^{rms}_{CSA\times CSA}$ and $\kappa^{rms}_{CSA\times iso}$, with the pulse fraction f. This figure is discussed in the following subsections.

2.3. BABA recoupling

Different variants of the BABA scheme have been proposed [8]. As the ^{31}P–^{31}P dipolar coupling constants are moderate ($|b|/2\pi \leqslant 900$ Hz between phosphate groups), the optimal τ_{exc} and τ_{rec} values are larger than 10 rotor periods at high MAS frequencies ($\nu_R \geqslant 30$ kHz). Therefore, super-cycled BABA sequences can be employed. Here, we used the BABA-4 sequence [8], spanning four rotor periods and depicted in Fig. 1b. This sequence corresponds to the $(R2^0_2)2^1 = (R2^0_2)_0(R2^0_2)_{180}$ symmetry, using the basic inversion element $\mathscr{R} = \pi/2_0 - \tau - \pi/2_0 - \pi/2_{90} - \tau - \pi/2_{270}$. Here, the standard notations for rf pulse and super-cycle are used [34,44]. ξ_ϕ indicates a rectangular, resonant rf pulse with flip angle ξ and phase ϕ. The rf pulses are assumed to be strong and short and the delay τ is adjusted so that the basic element $\mathscr{R}$ lasts one rotor

period. The $(R2_2^0)2^1$ symmetry implements both 0Q and 2Q dipolar recoupling and suppresses the unwanted CSA and isotropic chemical shift terms to first-order. The scaling factors for DD coupling 0Q term in $\overline{H}^{(1)}$ vanish in the limit of strong rf field, i.e., low pulse fraction f, whereas the scaling factor κ^{rms}_{DD2Q} of 2Q operators tends to $\sqrt{2}/\pi$ in this limit. Fig. 2a shows that BABA-4 leads to much larger κ^{rms}_{DD2Q} values than the other recoupling methods. Thus, BABA-4 requires short optimal recoupling times. This advantage comes at the expense of significant $\kappa^{rms}_{CSA\times CSA}$ and $\kappa^{rms}_{CSA\times iso}$ values, even when the pulse fraction f tends to zero (see Fig. 2b and c). These high second-order cross-terms partly explain the high sensitivity of BABA-4 to CSA and resonance offsets. These CSA and δ_{iso} interferences preclude the use of BABA-4 for ^{31}P nuclei at large static magnetic fields.

2.4. SPIP recoupling

The SPIP recoupling sequence, depicted in Fig. 1c, was recently introduced in order to recouple the ^{1}H–^{1}H dipolar couplings at high MAS frequency [39]. It is constructed from the $R2_2^1$ symmetry-based sequence employing a composite π pulse $\mathscr{R} = \theta_0\pi_0\theta_{180}$ as basic element. The basic $R2_2^1$ symmetry achieves both 0Q and 2Q homonuclear dipolar recoupling but does not suppress all offset and CSA terms in the first-order AHT. These unwanted CSA and offset terms can be removed by applying a block super-cycle, which consists in an overall phase shift of rf pulses from the middle of the τ_{exc} and τ_{rec} delays. This super-cycle is similar to that described by Mali et al. in the case of homonuclear dipolar recoupling of quadrupolar nuclei [40]. Therefore, when these delays span $4 \times p$ rotor periods, the SPIP sequence corresponds to $(R2_2^1)^p(R2_2^{-1})^p = R2p^p_{2p}R2p^{-p}_{2p}$ symmetry. This symmetry leads to a better suppression of CSA interferences than the usual phase inversion super-cycle $(R2_2^1R2_2^{-1})^p$ (see Fig. 4 in Ref. [39]). However, we have verified with the 'C and R symmetries' Mathematica package that the first- and second-order AHT scaling factors of $(R2_2^1)^p(R2_2^{-1})^p$ and $(R2_2^1R2_2^{-1})^p$ sequences are identical up to $p = 4$. The advantage of the block super-cycle over the phase inversion super-cycle may arise from a better suppression of CSA and offset contributions in the Magnus expansion terms with order greater than 2.

Fig. 2a shows that the κ^{rms}_{DD2Q} scaling factor for SPIP tends to zero in the limit of low pulse fraction and is globally much lower than that of BABA-4. Therefore, SPIP employs longer recoupling delays than BABA-4. Simultaneously, $\kappa^{rms}_{CSA\times CSA}$ and $\kappa^{rms}_{CSA\times\ iso}$ cross-terms scaling factors are also vanishing in the limit of strong rf field, i.e., low f values ($f < 0.1$, see Fig. 2b and c). The choice of the pulse fraction results from a compromise between the suppression of the CSA and the irreversible losses.

If Fig. 2 properly predicts the dependence of the optimal efficiency and recoupling time with the f value, it fails in explaining why SPIP sequence with $f > 0.2$ ($\nu_1 < 2.5\nu_R$) is more robust to CSA and offset than BABA sequences. This higher robustness of SPIP over BABA was demonstrated previously (see Figs. 2, 5 and 7 in Ref. [39]). Furthermore, it is confirmed in the case of ^{31}P nuclei experiencing large CSA by the comparison of Fig. 3a and c. Conversely Fig. 2 shows that the $\kappa^{rms}_{CSA\times CSA}$ and $\kappa^{rms}_{CSA\times iso}$ scaling factors of SPIP scheme are larger than those of BABA-4, when f exceeds 0.2. This discrepancy clearly evidences the limitations of the AHT up to the second order, when the ^{31}P CSA is larger than the spinning speed. In that case, only numerically exact simulations allow a quantitative assessment of CSA interferences.

Windowless SPIP basic element was used in the case of ^{1}H–^{1}H dipolar recoupling in order to decrease the irreversible losses, since the $T_{1\rho}$ relaxation times of ^{1}H nuclei are significantly larger than the T_2' times. This does not hold for ^{31}P nuclei and the sandwiching θ pulses can be replaced by 'window' intervals, during which no rf field is applied.

2.5. $BR2_2^1(\tau\pi\tau)$ recoupling

The substitution of the θ pulses in SPIP by windows leads to the recoupling sequences depicted in Fig. 1d. This sequence originating from the $R2_2^1$ symmetry employs a windowed basic element $\mathscr{R} = \tau - \pi_0 - \tau$. The delay τ is adjusted so that the basic element $\mathscr{R}$ lasts one rotor period. The block super-cycle is identical to that of SPIP, and hence the sequence is called $BR2_2^1(\tau\pi\tau)$ in the following. Therefore, $BR2_2^1(\tau\pi\tau)$ sequence provides 0Q and 2Q dipolar recoupling, while suppressing the unwanted CSA and offset terms to first-order. As for SPIP, κ^{rms}_{DD2Q}, $\kappa^{rms}_{CSA\times CSA}$ and $\kappa^{rms}_{CSA\times iso}$ scaling factors for $BR2_2^1(\tau\pi\tau)$ tend to zero for low f values (see Fig. 2). Hence, large rf fields are required in order to suppress the CSA and offset interferences. Compared to SPIP, $BR2_2^1(\tau\pi\tau)$ yields larger κ^{rms}_{DD2Q} factor and smaller $\kappa^{rms}_{CSA\times CSA}$ and $\kappa^{rms}_{CSA\times iso}$ interference terms (see Fig. 2). Thus, $BR2_2^1(\tau\pi\tau)$ requires shorter recoupling time than SPIP and is much more robust to CSA and offset. Both features are advantageous in the case of ^{31}P nuclei, which experience moderate DD couplings and strong CSAs.

2.6. [fp-RFDR] recoupling

The [fp-RFDR] sequence is depicted in Fig. 1e. The usual version of fp-RFDR is constructed from $R4_4^1$ symmetry with an overall 45° phase shift and employs the same basic element as $BR2_2^1(\tau\pi\tau)$ [32,34]. This symmetry achieves 0Q dipolar recoupling and removes the CSA and offset interferences to first-order. The unwanted terms can be further suppressed by using super-cycle, such as XY-8 and XY-16 [49]. The fp-RFDR sequence with XY-16 super-cycle corresponds to the symmetry $(R4_4^{-1}R4_4^1)2^1 = (R4_4^{-1}R4_4^1)_0(R4_4^{-1}R4_4^1)_{180}$ with an overall 45° phase shift, while the XY-8 super-cycle corresponds to $(R4_4^{-1}R4_4^1)_{45}$. The insertion of bracketing $\pi/2$-pulses at the beginning and at the end of fp-RFDR yields the [fp-RFDR] scheme and allows for the excitation of 2QCs. Compared to $BR2_2^1(\tau\pi\tau)$ and SPIP, [fp-RFDR] benefits from larger κ^{rms}_{DD2Q} factor and lower $\kappa^{rms}_{CSA\times CSA}$ and $\kappa^{rms}_{CSA\times iso}$ values (see Fig. 2). Therefore, an analysis based on AHT limited to the second-order predicts that [fp-RFDR] is more advantageous than BABA-4, SPIP and $BR2_2^1(\tau\pi\tau)$ in order to excite ^{31}P 2QCs at high magnetic field. This theoretical prediction will be compared with numerically exact simulations and experiments in the following sections.

3. Simulations with one isolated spin pair

In preparation for the experiments, we performed simulations with the SIMPSON software [50]. The powder averaging was per-

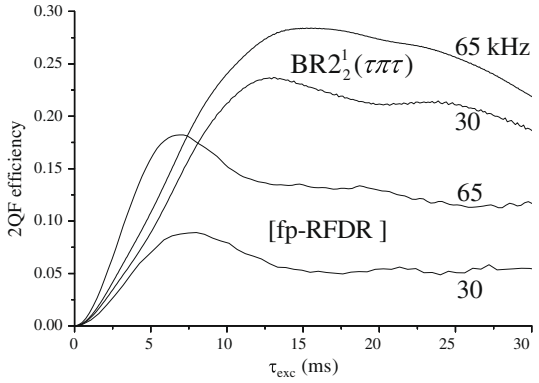

Fig. 4. Simulations of ^{31}P 1D 2QF build-up curves of one ^{31}P–^{31}P spin pair for two different recoupling sequences, [fp-RFDR] and $BR2_2^1(\tau\pi\tau)$, and two different MAS frequencies $\nu_R = 30$ and 65 kHz. Both ^{31}P nuclei experience large CSA ($\delta_{aniso} = 250$ ppm). The other simulation parameters are identical to those of Fig. 3.

formed using 11 γ angles and 256 crystallite orientations selected according to the REPULSION algorithm [51]. The performances of the recoupling schemes were compared in 1D 2QF experiments. The build-up of 2QCs may be estimated by acquiring 2QF NMR signals as a function of the intervals τ_{exc} and τ_{rec}. Different protocols can be used [11,31,36,38,52,53,14]. In the following, we will only describe the results obtained with the symmetric protocol, i.e., the two intervals τ_{exc} and τ_{rec} are both incremented but kept equal to each other: $\tau_{exc} = \tau_{rec}$. In Figs. 3–6, the vertical axes show the calculated 2QF efficiencies, defined as the ratio of the integral of 1D 2QF spectra to the integral of 1D spectrum obtained after $\pi/2$-pulse excitation. This definition gives efficiency twice smaller than that defined in Ref. [12]. Moreover, our excitation time τ_{exc} is equal to half that defined as 'excitation time' in this article [12].

We have performed the comparison of the four recoupling sequences (BABA-4, [fp-RFDR], SPIP and $BR2_2^1(\tau\pi\tau)$), on one isolated ^{31}P–^{31}P spin pair. The dipolar interaction was fixed to $b/(2\pi) = -263$ Hz, the magnetic field to $B_0 = 18.8$ T, the spinning speed to $\nu_R = 30$ kHz and both species were submitted to the same CSA. The rf irradiation was applied in the middle of these two resonances, which are separated by a small difference in isotropic chemical shifts of $\Delta\delta_{iso} = 2$ ppm. Fig. 3 compares the build-up curves of 2QF efficiencies as a function of the excitation time τ_{exc} for the four recoupling schemes and four different CSA values ($\delta_{aniso} = 0$, 80, 160 and 250 ppm) while the shielding tensor asymmetry parameter, η, is fixed to 0.1. It must be reminded that the

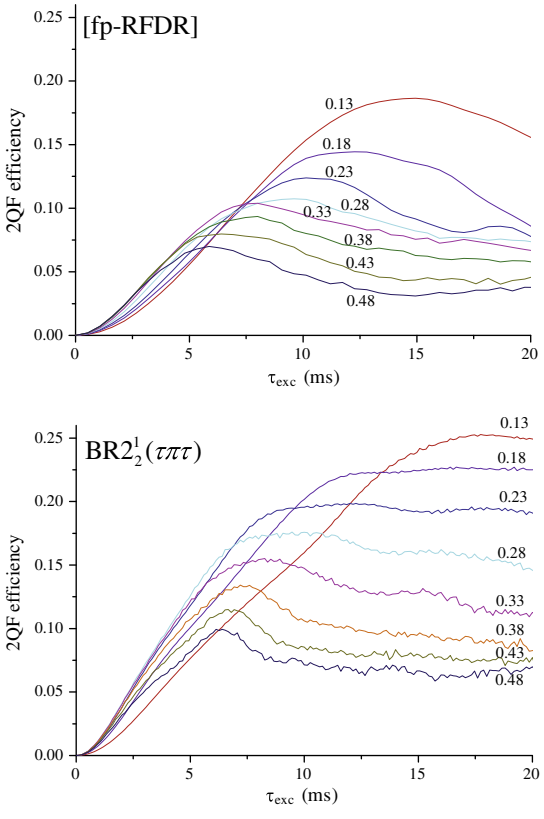

Fig. 5. Simulations of ^{31}P 1D 2QF build-up curves of one ^{31}P–^{31}P spin pair for [fp-RFDR] and $BR2_2^1(\tau\pi\tau)$ sequences with different f pulse fractions indicated in the figure. In that case, the maximal efficiencies are obtained for very long τ_{exc} and τ_{rec} values since the κ^{rms}_{DD2Q} factors tend to zero for small f fractions (see Fig. 2a). However, the build-up curves of Fig. 5 were calculated for an isolated spin pair, in the absence of relaxation. Experimentally, additional coherent and incoherent decay mechanisms can damp the 2QF efficiency for long recoupling time. Both ^{31}P nuclei experience large CSA ($\delta_{aniso} = 250$ ppm). The other simulation parameters correspond to those of Fig. 3.

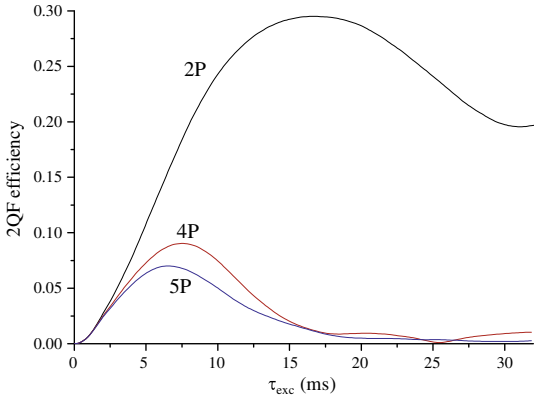

Fig. 6. Simulations of ^{31}P 1D 2QF build-up curves of the 3–6 correlation peak of octacalcium phosphate at $B_0 = 18.8$ T and $\nu_R = 30$ kHz. The spin system parameters are those of octacalcium phosphate [12]. We consider spin clusters comprising two (2P), four (4P) or five (5P) phosphorus nuclei. The $BR2_2^1(\tau\pi\tau)$ sequence was used with $f = 0.167$.

τ_{exc} and τ_{rec} values can only be multiples of $4T_R$ for BABA-4, SPIP and $BR2_2^1(\tau\pi\tau)$, and of $8T_R$ (XY-8) or $16T_R$ (XY-16) for [fp-RFDR].

Fig. 3 shows that for $\delta_{aniso} = 0$ ppm, the optimal excitation time, τ_{opt}, leading to maximal 2QF efficiency for the symmetric protocol, increases in the following order: BABA-4, [fp-RFDR], $BR2_2^1(\tau\pi\tau)$ and SPIP. This agrees with the relative magnitude of κ^{rms}_{DD2Q} scaling factors (see Fig. 2a) and shows the validity of AHT in this case. For ^{31}P–^{31}P dipolar recoupling at high MAS frequency, the τ_{opt} values are much larger than the minimal sampling period (4–$16T_R$). Under such condition, large κ^{rms}_{DD2Q} scaling factors and hence short τ_{opt} delays are advantageous since they allow decreasing the irreversible losses and thus increasing the experimental 2QF efficiency. Conversely, in the case of ^1H nuclei, which experience strong homonuclear DD couplings, low κ^{rms}_{DD2Q} scaling factors are required to sample easily the maxima of 2QF efficiency [39]. If the BABA sequence benefits from the shorter recoupling time, it is not able to manipulate efficiently spin species submitted to not negligible CSAs (Fig. 3a). This results from the large magnitude of $\kappa^{rms}_{CSA\times CSA}$ scaling factor (see Fig. 2b). The robustness to CSA of SPIP and [fp-RFDR] are similar, while $BR2_2^1(\tau\pi\tau)$ is the most robust sequence. The higher robustness of $BR2_2^1(\tau\pi\tau)$ was not predicted by the AHT up to second order, since the $\kappa^{rms}_{CSA\times CSA}$ scaling factor of $BR2_2^1(\tau\pi\tau)$ was larger than that of [fp-RFDR] (see Fig. 2b). This robustness may arise from a better suppression of CSA in the Magnus expansion terms $\overline{H}^{(i)}$ with $i \geqslant 3$. This result again illustrates the fact that the first- and the second-order terms do not suffice to assess CSA interferences when the ^{31}P CSA magnitude exceeds the inverse period of the sequence. In summary, $BR2_2^1(\tau\pi\tau)$ and [fp-RFDR] are the two most efficient methods for ^{31}P–^{31}P dipolar recoupling. $BR2_2^1(\tau\pi\tau)$ manifests higher robustness to CSA than [fp-RFDR], but requires longer recoupling time.

In Fig. 4, we have represented the build-up curves of $BR2_2^1(\tau\pi\tau)$ and [fp-RFDR], at fast and ultra-fast spinning speed ($\nu_R = 30$ and 65 kHz, respectively), for the previous ^{31}P–^{31}P spin pair with both nuclei submitted to a strong CSA of 250 ppm at 18.8 T. The maximum efficiency of both methods increases with spinning speed, and becomes approximately equal to its value observed without CSA (≈0.28) for $BR2_2^1(\tau\pi\tau)$ at $\nu_R = 65$ kHz. This result indicates a decrease of CSA interference with increasing MAS frequency. This is consistent with AHT since the Magnus expansion terms $\overline{H}^{(i)}$ with $i \geqslant 2$ decline with increasing MAS frequency. The fact that the detrimental effect of CSA can be suppressed with fast spinning, which is shown by simulations in Fig. 4, has already been demonstrated experimentally in the case of hydroxyapatite [58]. The 2QF effi-

ciency only reflects the integral of the whole spectra. Thus, the increase in intensity of the center bands is reinforced by the quasi-disappearance of spinning sidebands at 65 kHz. However, the experimental *S*/*N* ratios may not follow the same trend owing to the difference of sample volume between a 2.5 (ν_R = 30 kHz) and a 1.2–1.3 (ν_R = 65 kHz) mm rotors.

Fig. 5 shows a series of [fp-RFDR] and $BR2^1_2(\tau\pi\tau)$ build-up curves simulated for different f values. The MAS frequency is ν_R = 30 kHz, while the other simulation parameters correspond to those of Fig. 4. For both recoupling sequences, there is a decrease of the τ_{opt} delays for increasing f ratio. This results from the vanishing κ^{rms}_{DD2Q} scaling factors in the limit of low f, i.e., strong rf field (see Fig. 2a). Furthermore, the sensitivity to CSA increases with increasing f ratio since the $\kappa^{rms}_{CSA\times CSA}$ factors of [fp-RFDR] and $BR2^1_2(\tau\pi\tau)$ are increasing functions of f (see Fig. 2b and c). Therefore, the optimal rf field for [fp-RFDR] and $BR2^1_2(\tau\pi\tau)$ sequences depends on both the DD coupling, the CSA and the relaxation times. It must be noted that, for a given f value, the $BR2^1_2(\tau\pi\tau)$ method is always more efficient than [fp-RFDR].

4. Simulations of multi-spin interactions

Previous simulations were performed for an isolated spin pair. A problem, which is frequently encountered in ^{31}P NMR, is the damping of build-up curves obscuring possible informative oscillations. The damping results from incoherent processes, and coherent decay mechanisms, such as the dissipation of spin-order into multiple-spin coherences through the multiple DD ^{31}P–^{31}P couplings. The influence of relaxation damping on the dipolar coupling measurements may be reduced by using a constant-time procedure [11,31,36,38,52,53,14]. An example of coherent decay mechanism is the dipolar truncation phenomenon, which affects essentially all homonuclear dipolar recoupling sequences [54–56]. This means that long-range correlations between two nuclei are not visible when one of them is also involved in a short-range correlation with a third nucleus. However, coherent decay processes are not limited to dipolar truncation (one strong and one weak dipolar interactions). For instance, it also occurs as long as there are more than two neighboring spins with similar dipolar interactions. In the case of the P_2S_7 group in $Ag_7P_3S_{11}$, which only presents two different ^{31}P species, it has been shown that the built-up curve is mainly influenced by the distance between the first-nearest neighbors (356 pm), because the distance to the second-nearest neighbors (501 pm) are 1.4 larger than that between the first-nearest neighbors [11]. In contrast, in a recent article on ^{31}P [fp-RFDR] correlations in octacalcium phosphate [12], it has been shown that this signal decrease related to multi-spin interactions can be quite severe in case of several dipolar interactions of similar amplitudes.

Fig. 6 evidences similar decays for the $BR2^1_2(\tau\pi\tau)$ build-up curves of P_3–P_6 (3–6) correlation peaks of octacalcium phosphate. The spin system parameters are those already reported for this compound [12]. In particular, the inter-nuclear distances are d_{23} = 401.7, d_{36} = 420.6, d_{56} = 435.0, d_{26} = 495.1 and d_{22} = 683.5 pm. The build-up curves were simulated for spin clusters containing either 2 (P_3, P_6), 4 (P_3, P_6 and two P_2), or 5 (P_3, P_6, two P_2 and P_5) phosphorous atoms; called clusters 2P, 4P or 5P, respectively [12]. We have observed the same behavior for the four sequences whatever the spinning speed. Moreover, the $BR2^1_2(\tau\pi\tau)$ build-up curves calculated at ν_R = 30 kHz (see Fig. 6) are very similar to those calculated with [fp-RFDR] sequence at ν_R = 10 kHz

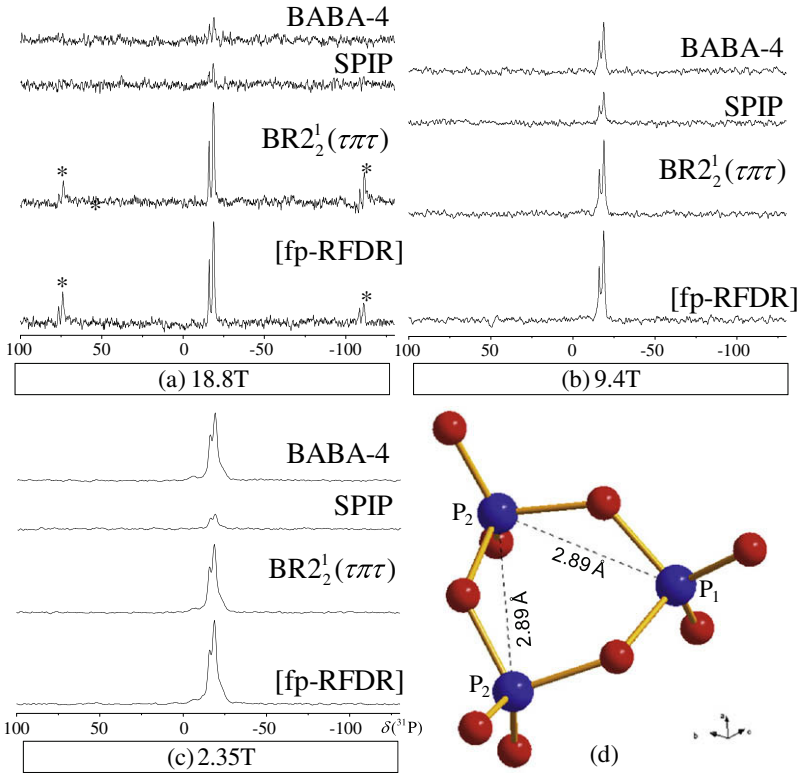

Fig. 7. ^{31}P 1D 2QF spectra of $Na_3P_3O_9$ sample employing various B_0 fields and recoupling sequences: BABA-4, SPIP, $BR2^1_2(\tau\pi\tau)$ and [fp-RFDR]. (a) Spectra at B_0 = 18.8 T and ν_R = 30 kHz. The $\tau_{exc} = \tau_{rec}$ and f values are equal to 400 μs and 0.46 for BABA-4, 2666 μs and 0.23 for SPIP, 1333 μs and 0.23 for $BR2^1_2(\tau\pi\tau)$, 1066 μs and 0.23 for [fp-RFDR]. The rf field of hard $\pi/2$ pulse is 84 kHz. (b) Spectra at B_0 = 9.4 T and ν_R = 30 kHz. The $\tau_{exc} = \tau_{rec}$ and f values are equal to 533 μs and 0.48 for BABA-4, 2133 μs and 0.275 for SPIP, 1600 μs and 0.275 for $BR2^1_2(\tau\pi\tau)$ and [fp-RFDR]. The rf field of hard $\pi/2$ pulse is 84 kHz. (c) Spectra at B_0 = 2.35 T and ν_R = 20 kHz. The $\tau_{exc} = \tau_{rec}$ and f values are equal to 551 μs and 0.30 for BABA-4, 3310 μs and 0.15 for SPIP, 2100 μs and 0.15 for $BR2^1_2(\tau\pi\tau)$ and [fp-RFDR]. The rf field of hard $\pi/2$ pulse is 66 kHz. The stars in (a) indicate spinning sidebands.

[12]. This dramatic decrease in efficiency increases with the size of the cluster. It has been explained by the fact that 'the passive spins in close proximity provide a strong dipolar dephasing of the excited 2Q coherences' [12]. It can be verified that this effect is independent from the spinning speed, and efficiencies obtained at $\nu_R = 30$ or 65 kHz (not shown) are similar. As a consequence, distance measurement by DQ spectroscopy in homonuclear spin systems is applicable only if the two-spin approximation holds. This is the case in ^{13}C–^{13}C experiments performed on biological molecules, because dipolar interactions between second neighbors are smaller by a factor of at least 5 with respect to those between first neighbors. However, this may not be the case in three-dimensional networked materials.

5. Experimental 1D results

We have tested the BABA-4, SPIP, $BR2^1_2(\tau\pi\tau)$ and [fp-RFDR] experiments on $Na_3P_3O_9$. The experiments were performed on three (2.35, 9.4 and 18.8 T) Bruker Avance-II spectrometers equipped with 2.5 (9.4 and 18.8 T) or 3.2 (2.35 T) mm MAS probes.

Sodium trimetaphosphate, $Na_3P_3O_9$, was synthesized as described in Ref. [57] including partial ^{17}O enrichment. It crystallizes in the orthorhombic *Pmcn* space group with four formula units per unit cell [57]. The basic unit of $Na_3P_3O_9$ is composed of two crystallographically distinct sodium sites, two phosphorous sites and six oxygen sites. The ^{31}P MAS spectra exhibit two resonances P_1 at −16.0 ppm and P_2 at −18.8 ppm, in a 1:2 ratio, in good agreement with crystallographic data. The ^{31}P–^{31}P inter-nuclear distances and dipolar interactions are equal to: $d_{11} = 410$, $d_{22} \approx d_{12} \approx 289$ pm, i.e., $b_{11}/(2\pi) = -283$, $b_{22}/(2\pi) \approx b_{12}/(2\pi) \approx -812$ Hz. The basic anionic unit is composed of a ring of three phosphate groups (Fig. 7d). Following the conventional notation, all phosphate entities in $Na_3P_3O_9$ are noted Q^2 because they are connected to two other phosphate groups. The CSAs of these two ^{31}P species, evaluated from their sideband patterns, are approximately equal to $\delta_{aniso} \approx 155$ (P_1) and 165 (P_2) ppm. At 18.8 T, these broadenings are very large and equal to 50 (P_1) and 53 (P_2) kHz. The 1D 2QF spectra of $Na_3P_3O_9$, recorded with $\nu_R = 30$ kHz at 18.8 T are represented in Fig. 7a. The signal is about five times weaker with SPIP and BABA-4 than with [fp-RFDR] and $BR2^1_2(\tau\pi\tau)$. These results evidence the higher robustness of [fp-RFDR] and $BR2^1_2(\tau\pi\tau)$ to CSA. Furthermore, the relative 2QF efficiencies approximately correspond to those predicted from numerical simulations (see Fig. 3), especially if we take into account the irreversible losses that are very important for SPIP, and not negligible for $BR2^1_2(\tau\pi\tau)$, owing to their recoupling time, $\tau_{exc} + \tau_{rec}$, longer than that of [fp-RFDR]. When decreasing the spinning speed to $\nu_R = 20$ kHz, only the $BR2^1_2(\tau\pi\tau)$ sequence gave a good efficiency (*not shown*), because the CSAs were then not enough averaged by BABA-4 and [fp-RFDR] sequences, and the losses still remained very important with SPIP. In order to test the influence of the CSAs, we performed the same 1D experiments on $Na_3P_3O_9$ at lower fields, 9.4 T (Fig. 7b) and 2.35 T (Fig. 7c), which means that the CSAs were scaled down (in Hz) by a factor of 2 and 8, respectively, with respect to 18.8 T. At 9.4 T, we used the same spinning speed of 30 kHz, which means that the only difference between experiments performed at 9.4 and 18.8 T resides in the CSAs. We do not have a 2.5-mm probe operating at 2.35 T, and the spinning speed was thus limited to 20 kHz with a 3.2-mm probe. One observes a merging of the efficiencies of BABA-4, $BR2^1_2(\tau\pi\tau)$ and [fp-RFDR], with decreasing CSAs. However, SPIP signal remains weak at 2.35 T, owing to long recoupling time and hence large irreversible losses. This merging effect was previously shown by simulations performed with large or moderate CSAs (Fig. 3). Two opposite effects can be observed when increasing the magnetic field (Fig. 7a–c): the *S*/*N* ratio decreases and the resolution is enhanced. The first effect is related to the very long T_{1z} relaxation time of phosphorous magnetization, which increases with the magnetic field (≈200, 600, 1000 s at 2.35, 9.4, 18.8 T, respectively). With such long relaxation times, accumulations were performed on full rotor samples with initial pre-saturation followed by a constant delay of Δt. We have used similar delays in all experiments ($\Delta t \approx 50$ s), which leads to a decrease of the *S*/*N* ratio with increasing field. Moreover, the sample volume at 2.35 T was ca. 3 times larger than that used at 9.4 and 18.8 T, which also leads to a much better *S*/*N* ratio at that field. The second effect is related to the resolution 'enhancement' observed with increasing magnetic field. This enhancement stems from the line-width nature of $Na_3P_3O_9$. This well-crystallized compound shows very narrow chemical shift distribution. Moreover, ^{31}P is submitted to $^2J_{POP}$ that ranges between 10 and 30 Hz [6]. Finally, one can observe a very complex $^1J_{PO}$ multiplet structure ($^1J_{PO}$ coupling is around 120 Hz in this compound [26]) mostly restricted around the base of the resonance because of partial ^{17}O enrichment. We have estimated the two resonance line-widths avoiding the $^1J_{PO}$ coupling multiplet, and have observed line-widths of ca. 55 ± 5, 65 ± 5, 150 ± 10 Hz for P_1 and 55 ± 5, 175 ± 15, 300 ± 20 Hz for P_2,

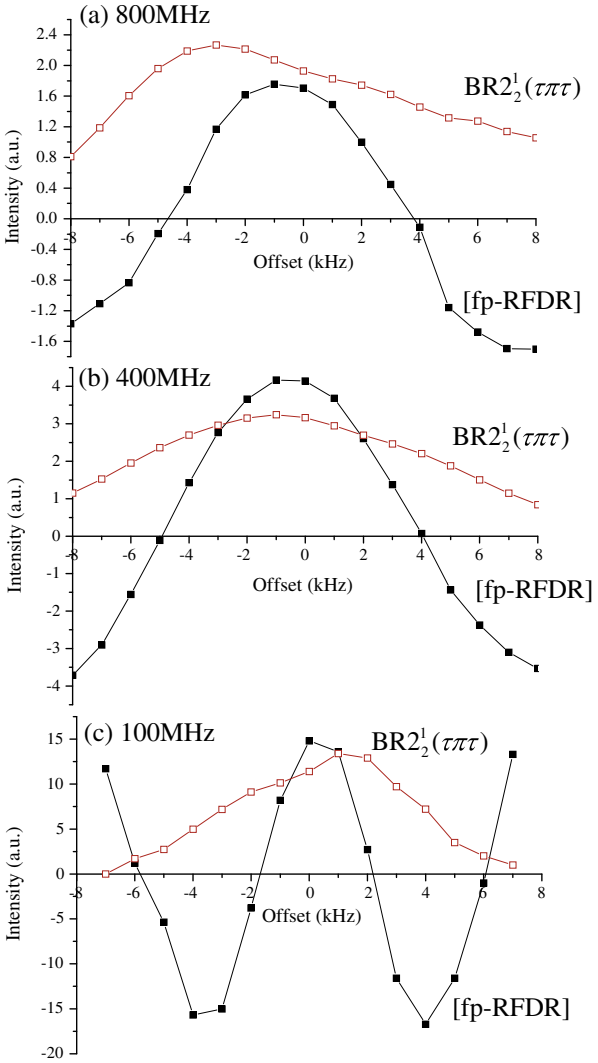

Fig. 8. ^{31}P 1D 2QF signal in $Na_3P_3O_9$ sample, as a function of the offset irradiation, observed when using [fp-RFDR] and $BR2^1_2(\tau\pi\tau)$ sequences, with $\nu_R = 30$ kHz and $B_0 = 18.8$ T (a) or 9.4 T (b) and $\nu_R = 20$ kHz and $B_0 = 2.35$ T (c). The intensity is given in arbitrary units (a.u.). The other experimental parameters are those given in Fig. 7 caption.

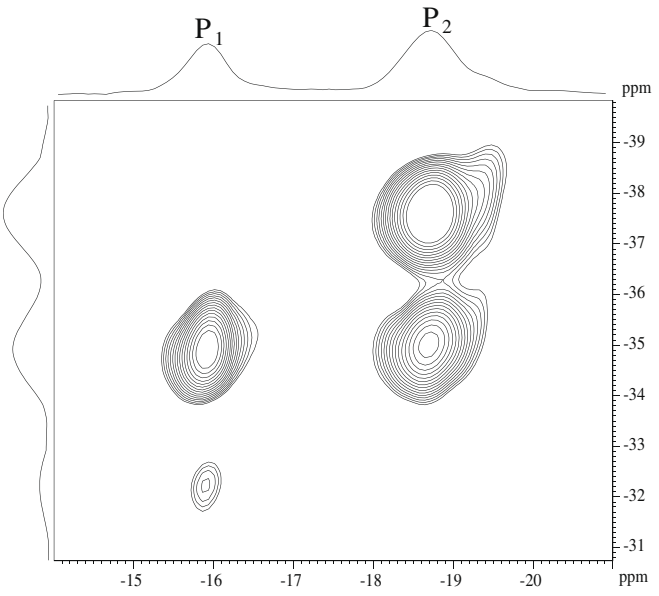

Fig. 9. ^{31}P 2D 2Q–1Q *D*-HOMCOR spectrum of $Na_3P_3O_9$ recorded at 18.8 T with ν_R = 30 kHz. The dipolar recoupling sequence is $BR2^1_2(\tau\pi\tau)$ with $\tau_{exc} = \tau_{rec}$ = 1333 μs and f = 0.23. The rf nutation frequency of $\pi/2$ pulses is 84 kHz. This spectrum only represents a restricted region without any sidebands. The number of scans is 16, recycling delay is Δt = 90 s, 50 points in t_1 dimension with Δt_1 = 200 μs. The total experimental time is 20 h. The contour levels are separated every 5%.

at 2.35, 9.4 and 18.8 T, respectively. Therefore, we can deduce that at 2.35 T the two line-widths are dominated by the scalar ^{31}P–^{31}P triplets due to $^2J_{POP}$ couplings (Fig. 7d), and hence that the chemical shift distribution is limited to ca. 0.20 (P_1) and 0.50 (P_2) ppm. At 9.4 T, these values correspond to the P_1 line-width, but the P_2 resonance must also be broadened by another process, certainly incoherent. At 18.8 T, a larger incoherent broadening is observed for both species. Globally, by comparing the ratio between the line-widths and the fields, we observe a significant resolution enhancement when going from 2.35 to 9.4 T, but only the bases of the resonance are better resolved between 9.4 and 18.8 T spectra (Fig. 7a and b).

We have also measured on $Na_3P_3O_9$ the offset sensitivity of the two most efficient sequences, namely [fp-RFDR] and $BR2^1_2(\tau\pi\tau)$, at three magnetic fields, 18.8 T (Fig. 8a), 9.4 T (Fig. 8b) and 2.35 T (Fig. 8c). The offset full-width at half-height (FWHH) of $BR2^1_2(\tau\pi\tau)$ is always at least the double of that observed for [fp-RFDR]: FWHH($BR2^1_2(\tau\pi\tau)$)/FWHH([fp-RFDR]) 46/18, 80/38 and 200/68 ppm, as shown in Fig. 8a, b and c, respectively. For most samples, this chemical shift range is quite sufficient below 9.4 T, but may be slightly too small at 18.8 T, especially for [fp-RFDR].

Current 1.3 mm MAS probes for 18.8 T spectrometers are not yet able to tune at ^{31}P Larmor frequency, and hence we have not been able to compare simulations performed at ν_R = 65 kHz with experimental data.

6. Experimental 2D results

Although 2QF experiments are useful to test the efficiency and the robustness of the recoupling sequences, they only allow determining whether a spin species is subject to dipole–dipole couplings, but the identity of the other spins involved in the couplings remains unknown. In order to identify the two spin species forming a dipolar-coupled pair, the 2QF experiment has to be extended to a 2D 2Q–1Q *D*-HOMCOR experiment. We have recorded the 2D 2Q–1Q $BR2^1_2(\tau\pi\tau)$ spectrum of $Na_3P_3O_9$ at 18.8 T and ν_R = 30 kHz (Fig. 9). Under MAS, the two ^{31}P resonances are well resolved without overlapping. The NMR parameters of these ^{31}P species have been deduced from the spinning sideband patterns: {δ_{iso} (ppm), δ_{aniso} (ppm), η} = {−16.0, −155, 0.06} for P_1; and {−18.8, −165, 0.1} for P_2. Chemical shift separation between the two species is small (2.8 ppm), but both species are submitted to a large CSA: 50 and 53 kHz at 18.8 T, for P_1 and P_2, respectively. The spinning speed was thus insufficient to avoid sidebands in the spectrum (Fig. 7a). The 2–2 auto-peak exhibits a large signal, whereas that for 1–1 is small, in agreement with the dipolar coupling constants: $b_{11}/(2\pi)$ = −283 Hz and $b_{22}/(2\pi)$ = −810 Hz values.

7. Conclusions

We have demonstrated that a new simple pulse-sequence, $BR2^1_2(\tau\pi\tau)$, can be applied for double-quantum NMR experiments on spin-1/2 nuclei submitted to very large CSAs. The method, which is a modified version of the rotor-synchronized $R2^1_2$ sequence, is efficient and robust to both CSA and offset. In the same way as [fp-RFDR], $BR2^1_2(\tau\pi\tau)$ uses finite π pulses the amplitude of which is moderate and does not require stringent conditions. The main difference between the two sequences resides in the much more robust behavior of $BR2^1_2(\tau\pi\tau)$ with respect to off-resonance irradiation.

Presently, the main limitation of all homonuclear dipolar methods is related to the coherent decay processes resulting from multiple dipolar interactions. A well-known example of such phenomenon is dipolar truncation, which prevents the observation of long-range correlations between two nuclei, when one of them is also involved in a short-range correlation with a third nucleus. However, there is also severe signal decay owing to multi-spin dipolar interactions with similar dipolar coupling constants. As a consequence, the determination of inter-nuclear distances in homonuclear spin systems is easily feasible only if the two-spin approximation holds.

A second limitation of these dipolar-based through-space methods is that unambiguous connectivity information cannot strictly be ensured, as opposed to through-bond *J*-based methods. However, it is well known that by a proper choice of a short dipolar recoupling time one may often obtain the same results as with through-bond methods, at the expense of the *S*/*N* ratio.

Acknowledgments

Authors are grateful for funding provided by Region Nord/Pas de Calais, Europe (FEDER), CNRS, French Minister of Science, FR-3050, USTL, ENSCL and Bruker BIOSPIN. The authors also thank Prof. Malcolm H. Levitt and Dr. Andreas Brinkmann for providing the 'C and R symmetries' Mathematica package, and Qiang Wang for helpful discussions. They also thank Prof. J.C.C. Chan for numerous stimulating discussions and for sending them his SIMPSON input file corresponding to octacalcium phosphate [12]. F.D. thanks the National Natural Science Foundation of China (20773159 and 20673139) and the National Basic Research Program of China (2009CB918600) for financial support.

Appendix A

The AHT and the symmetry-based selection rules entail that the first order average Hamiltonian, for the case of an isolated pair of homonuclear spin-1/2 nuclei, I_j and I_k, submitted to the fp-RFDR sequence, only contains the 0Q spherical tensor operator given by $T^{jk}_{2,0} = (3I_{zj}I_{zk} - \boldsymbol{I}_j \cdot \boldsymbol{I}_k)/\sqrt{6}$

$$\overline{H}^{(1)}(\text{fp-RFDR}) = \left(\sum_m \bar{\omega}^{jk}_{2m20}(\text{fp-RFDR})\right) T^{jk}_{2,0} \qquad \text{(A1)}$$

The complex amplitude of the recoupled 0Q homonuclear dipolar interaction is expressed as a sum of many rotational components $\bar{\omega}^{jk}_{2m20}$(fp-RFDR) with $m = \pm1, \pm2$. The amplitude $\bar{\omega}^{jk}_{2m20}$(fp-RFDR) can be expressed as follows

$$\bar{\omega}^{jk}_{2m20}(\text{fp-RFDR}) = \sqrt{6} b_{jk} \kappa_{2m20}(\text{fp-RFDR}) d^2_{0m}(\beta_{PR}) \times \exp\{-\mathrm{i}m(\gamma_{PR} + \alpha^0_{RL} - \omega_R t^0)\} \quad \text{(A2)}$$

where b_{jk} is the dipolar coupling constant between nuclei j and k. The scaling factors κ_{2m20} (fp-RFDR) can be computed in the 'C and R symmetries' Mathematica package. The Euler angles $\{\beta_{PR}, \gamma_{PR}\}$ relate the inter-nuclear j–k axis to the rotor-fixed frame. $d^2_{0m}(\beta_{PR})$ is a reduced Wigner matrix element, α^0_{RL} defines the initial rotor position, while ω_R and t^0 refer to the angular spinning frequency and the starting time of the fp-RFDR sequence.

When the fp-RFDR sequence is bracketed by $\pi/2$ pulses (see Fig. 1e), the time evolution of the I_j I_k spin system during the excitation interval, τ_{exc}, can be described, at the first order, by the propagator

$$U = R_y\left(-\frac{\pi}{2}\right) \exp\{-\mathrm{i}\bar{H}^{(1)}(\text{fp-RFDR})\tau_{\text{exc}}\} R_y\left(\frac{\pi}{2}\right) = \exp\left\{-\mathrm{i}\tilde{H}^{(1)}([\text{fp-RFDR}])\tau_{\text{exc}}\right\} \quad \text{(A3)}$$

where the operator $R_y(\theta) = \exp(-\mathrm{i}\theta I_y)$, with $I_y = I_{jy} + I_{ky}$, performs a rotation of I spins through the angle θ about the y-axis. When the [fp-RFDR] sequence is employed during the reconversion interval, τ_{exc} has to be substituted by τ_{rec} in Eq. (A3). The first-order average Hamiltonian in the tilted rotating frame has the form

$$\tilde{H}^{(1)}([\text{fp-RFDR}]) = R_y\left(-\frac{\pi}{2}\right)\bar{H}^{(1)}(\text{fp-RFDR}) R_y\left(\frac{\pi}{2}\right) = \left(\sum_m \bar{\omega}^{jk}_{2m20}(\text{fp-RFDR})\right) R_y\left(-\frac{\pi}{2}\right) T^{jk}_{2,0} R_y\left(\frac{\pi}{2}\right) \quad \text{(A4)}$$

Furthermore, the rotation properties of spherical tensor operators entail

$$R_y\left(-\frac{\pi}{2}\right) T^{jk}_{2,0} R_y\left(\frac{\pi}{2}\right) = -\frac{1}{2} T^{jk}_{20} + \frac{1}{2}\sqrt{\frac{3}{2}}\left(T^{jk}_{2,2} + T^{jk}_{2,-2}\right) \quad \text{(A5)}$$

where $T^{jk}_{2,\pm2} = I^{\pm}_j I^{\pm}_k/2$ are 2Q spherical tensor operators. Eqs. (A4) and (A5) indicate that the [fp-RFDR] sequence achieves both 0Q and 2Q dipolar recoupling. Nevertheless, only the 2Q terms in $\tilde{H}^{(1)}([\text{fp-RFDR}])$ can excite 2QC from longitudinal polarization and are involved in 1D 2QF and 2D 2Q–1Q D-HOMCOR experiments. Thus, we only keep the 2Q part of $\tilde{H}^{(1)}([\text{fp-RFDR}])$ in the following, i.e.,

$$\tilde{H}^{(1)}_{2Q}([\text{fp-RFDR}]) = \frac{1}{2}\sqrt{\frac{3}{2}}\left(\sum_m \bar{\omega}^{jk}_{2m20}(\text{fp-RFDR})\right)\left(T^{jk}_{2,2} + T^{jk}_{2,-2}\right) \quad \text{(A6)}$$

The scaling factors, $\kappa_{2m2\pm2}$ ([fp-RFDR]), of the recoupled 2Q dipolar interaction in the case of [fp-RFDR] sequence can be defined in the same way as in the case of symmetry-based pulse sequences (see Eq. (47) in Ref. [43]). Hence, from Eqs. (A2) and (A6), we obtain

$$\kappa_{2m22}([\text{fp-RFDR}]) = \kappa_{2m2-2}([\text{fp-RFDR}]) = \frac{1}{2}\sqrt{\frac{3}{2}}\kappa_{2m20}(\text{fp-RFDR}) \quad \text{(A7)}$$

The corresponding rms scaling factor, $\kappa^{rms}_{\text{DD2Q}}([\text{fp-RFDR}])$, can be calculated from Eq. (4). Finally, using Eq. (A7), Eq. (4) is equivalent to Eq. (5).

References

[1] K. Karaghiosoff, Phosphorus-31 NMR, in: Encyclopedia of Nuclear Magnetic Resonance, Wiley, Chichester, 1996.

[2] H. Eckert, Amorphous materials, in: Encyclopedia of Nuclear Magnetic Resonance, Wiley, Chichester, 1996.

[3] A. Iuga, M. Spoerner, H.R. Kalbitzer, E. Brunner, Solid-state ^{31}P NMR spectroscopy of microcrystals of the Ras protein and its effector loop mutants: comparison between crystalline and solution state, J. Mol. Biol. 342 (2004) 1033–1040.

[4] A. Iuga, C. Ader, C. Gröger, E. Brunner, Applications of solid-state ^{31}P NMR spectroscopy, Annu. Rep. NMR Spectrosc. 60 (2006) 145–189.

[5] R.J. Iuliucci, B.H. Meier, A characterization of the linear P–O–P bonds in $M^{4+}(P_2O_7)$ compounds: bond-angle determination by solid-state NMR, J. Am. Chem. Soc. 120 (1998) 9059–9062.

[6] F. Fayon, G. Le Saout, L. Emsley, D. Massiot, Through-bond phosphorus–phosphorus connectivities in crystalline and disordered phosphates by solid-state NMR, Chem. Commun. 16 (2002) 1702–1703 .

[7] C. Jäger, M. Feike, R. Born, H.W. Spiess, Direct detection of connectivities in glasses by 2D NMR, J. Non-Cryst. Solids 180 (1994) 91–95.

[8] M. Feike, D.E. Demco, R. Graf, J. Gottwald, S. Hafner, H.W. Spiess, Broadband multiple-quantum NMR spectroscopy, J. Mag. Reson. Ser. A 122 (1996) 214–221.

[9] H. Geen, J. Gottwald, R. Graf, I. Schnell, H.W. Spiess, J.Y. Titman, Elucidation of dipolar coupling networks under magic-angle spinning, J. Magn. Reson. 125 (1997) 224–227.

[10] F. Fayon, D. Massiot, K. Suzuya, D.L. Price, J. Non-Cryst. Solids 180 (2001) 88–94.

[11] J. Schmedt auf der Günne, Distance measurements in spin-1/2 systems by ^{13}C and ^{31}P solid-state NMR in dense dipolar networks, J. Magn. Reson. 165 (2003) 18–32.

[12] Y.H. Tseng, Y. Mou, C.Y. Mou, J.C.C. Chan, Double-quantum NMR spectroscopy based on finite pulse RFDR, Solid State NMR 27 (2005) 266–270.

[13] V. Brodski, R. Peschar, H. Schenk, A. Brinkmann, E.R.H. van Eck, A.P.M. Kentgens, Structure of tetrakis(melaminium) bis(dihydrogenphosphate) monohydrogenphosphate trihydrate from X-ray powder diffraction and solid-state NMR spectroscopy, J. Phys. Chem. C 112 (2008) 12515–12523.

[14] I. Schnell, Dipolar recoupling in fast MAS solid-state NMR spectroscopy, Prog. Nucl. Magn. Reson. Spectrosc. 45 (2004) 145–207.

[15] B.H. Meier, W.L. Earl, Excitation of multiple quantum transitions under magic angle conditions: adamantane, J. Chem. Phys. 85 (1986) 4905–4911.

[16] B.H. Meier, W.L. Earl, Double-quantum filter for rotating solids, J. Am. Chem. Soc. 109 (1987) 7937–7941.

[17] R. Tycko, G. Dabbagh, Measurement of nuclear magnetic dipole–dipole couplings in magic angle spinning NMR, Chem. Phys. Lett. 173 (1990) 461–465.

[18] R. Tycko, G. Dabbagh, Double-quantum filtering in magic-angle-spinning NMR spectroscopy: an approach to spectral simplification and molecular structure determination, J. Am. Chem. Soc. 113 (1991) 9444–9448.

[19] T. Gullion, S. Vega, A simple magic angle spinning NMR experiment for the dephasing of rotational echoes of dipolar coupled homonuclear spin pairs, Chem. Phys. Lett. 194 (1992) 423–428;
A.E. Bennett, J.H. Ok, R.G. Griffin, S. Vega, Chemical-shift correlation spectroscopy in rotating solids: radio frequency-driven dipolar recoupling and longitudinal exchange, J. Chem. Phys. 96 (1992) 8624–8627.

[20] N.C. Nielsen, H. Bildsoe, H.J. Jakobsen, M.H. Levitt, Double-quantum homonuclear rotary resonance: efficient dipolar recovery in magic angle spinning, J. Chem. Phys. 101 (1994) 1805–1812.

[21] R. Verel, M. Baldus, M. Nijman, J.W.M. Vanos, B.H. Meier, Adiabatic homonuclear polarization in magic-angle spinning solid-state NMR, Chem. Phys. Lett. 280 (1997) 31–39;
R. Verel, M. Baldus, M. Ernst, B.H. Meier, A homonuclear spin-pair filter for solid-state NMR based on adiabatic-passage techniques, Chem. Phys. Lett. 287 (1998) 421–428.

[22] W. Sommer, D.E. Demco, S. Hafner, H.W. Spiess, Rotation-synchronized homonuclear dipolar decoupling, J. Magn. Reson. Ser. A 116 (1995) 36–45.

[23] R. Graf, D.E. Demco, J. Gottwald, S. Hafner, H.W. Spiess, Dipolar couplings and internuclear distances by double-quantum nuclear magnetic resonance spectroscopy of solids, J. Chem. Phys 106 (1997) 885–895.

[24] M. Hohwy, H.J. Jakobsen, M. Edén, M.H. Levitt, N.C. Nielsen, Broadband dipolar recoupling in the nuclear magnetic resonance of rotating solids: a compensated C7 pulse sequence, J. Chem. Phys. 108 (1998) 2686–2694.

[25] C.M. Rienstra, M.E. Hatcher, L.J. Mueller, B. Sun, S.W. Fesik, R.G. Griffin, Efficient multispin homonuclear double-quantum recoupling for magic-angle spinning NMR: ^{13}C–^{13}C correlation spectroscopy of U–^{13}C–erythromycin A, J. Am. Chem. Soc. 12 (1998) 10602–10612.

[26] M. Carravetta, M. Edén, X. Zhao, A. Brinkmann, M.H. Levitt, Symmetry principles for the design of radiofrequency pulse sequences in the nuclear magnetic resonance of rotating solids, Chem. Phys. Lett. 321 (2000) 205–215.

[27] M. Baldus, M. Tomaselli, B.H. Meier, R.R. Ernst, Broadband polarization-transfer experiments for rotating solids, Chem. Phys. Lett. 230 (1994) 329–336;
M. Baldus, B.H. Meier, Broadband polarization transfer under magic-angle spinning: application to total through-space correlation NMR spectroscopy, J. Magn. Reson. 128 (1997) 172–193.

[28] R. Tycko, G. Dabbagh, Measurement of nuclear magnetic dipole–dipole couplings in magic angle spinning NMR, Chem. Phys. Lett. 173 (1990) 461–465;
R. Tycko, G. Dabbagh, Double-quantum filtering in magic angle spinning NMR spectroscopy: an approach to spectral simplification and molecular structure determination, J. Am. Chem. Soc. 113 (1991) 9444–9448.

[29] D.M. Gregory, D.J. Mitchell, J.A. Stringer, S. Kiihne, J.C. Shiels, J. Callahan, M.A. Mehta, G.P. Drobny, Windowless dipolar recoupling: the detection of weak dipolar couplings between spin-1/2 nuclei with large chemical-shift anisotropies, Chem. Phys. Lett. 246 (1995) 654–663;
D.M. Gregory, G.M. Wolfe, T.P. Jarvie, J.C. Shiels, G.P. Drobny, Double-quantum filtering in magic-angle spinning NMR spectroscopy applied to DNA oligomers, Mol. Phys. 89 (1996) 1835–1849.
[30] A. Brinkmann, M. Edén, M.H. Levitt, Synchronous helical pulse sequences in magic-angle spinning nuclear magnetic resonance: double quantum recoupling of multiple-spin systems, J. Chem. Phys. 112 (2000) 8539–8554.
[31] M. Carravetta, M. Eden, O.G. Johannessen, H. Luthman, P.J.E. Verdegem, J. Lugtenburg, A. Sebald, M.H. Levitt, Estimation of carbon–carbon bond lengths and medium-range inter-nuclear distances by solid-state nuclear magnetic resonance, J. Am. Chem. Soc. 123 (2001) 10628–10638.
[32] Y. Ishii, ^{13}C–^{13}C dipolar recoupling under very fast magic angle spinning in solid state nuclear magnetic resonance: applications to distance measurements, spectral assignments and high-throughput secondary-structure determination, J. Chem. Phys. 114 (19) (2001) 8473–8483.
[33] F.J. Blanco, R. Tycko, Determination of polypeptide backbone dihedral angles in solid state NMR by double quantum ^{13}C chemical shift anisotropy measurements, J. Magn. Reson. 149 (2001) 131–138.
[34] M.H. Levitt, Encyclopedia of Nuclear Magnetic Resonance, Wiley, Chichester, 2002. pp. 165–196.
[35] M. Edén, Enhanced symmetry-based dipolar recoupling in solid-state NMR, Chem. Phys. Lett. 378 (2003) 55–64.
[36] P.E. Kristiansen, M. Carravetta, W.C. Lai, M.H. Levitt, A robust pulse sequence for the determination of small homonuclear dipolar couplings in magic-angle spinning NMR, Chem. Phys. Lett. 390 (2004) 1–7.
[37] M. Edén, D. Zhou, J. Yu, Improved double-quantum NMR correlation spectroscopy of dipolar-coupled quadrupolar spins, Chem. Phys. Lett. 431 (2006) 397–403.
[38] P.E. Kristiansen, M. Carravetta, J.D. van Beek, W.C. Lai, M.H. Levitt, Theory and applications of supercycled symmetry-based recoupling sequences in solid-state NMR, J. Chem. Phys. 12 (2006) 234510–234519.
[39] B. Hu, Q. Wang, O. Lafon, J. Trébosc, F. Deng, J.P. Amoureux, Robust and efficient spin-locked symmetry-based double-quantum homonuclear dipolar recoupling for probing ^{1}H–^{1}H proximity in the solid state, J. Magn. Reson. 198 (2009) 41–48.
[40] G. Mali, G. Fink, F. Taulelle, Double-quantum homonuclear correlation magic angle spinning nuclear magnetic resonance spectroscopy of dipolar-coupled quadrupolar nuclei, J. Chem. Phys. 120 (2004) 2835–2845.
[41] J. Schmedt auf der Günne, H. Eckert, High-resolution double-quantum ^{31}P NMR: a new approach to structural studies of thiophosphates, Chem. Eur. J. 4 (1998) 1762–1767.
[42] M.J. Potrzebowski, J. Gajda, W. Ciesielski, I.M. Montesinos, Distance measurements in disodium ATP hydrates by means of ^{31}P double quantum two-dimensional solid-state NMR spectroscopy, J. Magn. Reson. 179 (2006) 171–173.
[43] A. Brinkmann, M.H. Levitt, Symmetry principles in the nuclear magnetic resonance of spinning solids: heteronuclear recoupling by generalized Hartmann–Hahn sequences, J. Chem. Phys. 115 (2001) 357–384.
[44] A. Brinkmann, M. Eden, Second order average Hamiltonian theory of symmetry-based pulse schemes in the nuclear magnetic resonance of rotating solids: application to triple-quantum dipolar recoupling, J. Chem. Phys. 120 (2004) 11726.
[45] W. Magnus, On the exponential solution of differential equations for linear operator, Commun. Pure Appl. Math. 7 (1954) 649–673.
[46] I. Marin-Montesinos, D.H. Brouwer, G. Antonioli, W.C. Lai, A. Brinkmann, M.H. Levitt, Heteronuclear decoupling interference during symmetry-based homonuclear recoupling in solid-state NMR, J. Magn. Reson. 177 (2005) 307–317.
[47] (a) Wolfram Research Inc., Champaign, Illinois, USA, Mathematica 6, 2007. Available from: <http://reference.wolfram.com/mathematica/ref>.;
(b) 'C and R symmetries' Mathematica package written by M.H. Levitt and A. Brinkmann. Available from: <http://www.mhl.soton.ac.uk/public/Main/software/CandRsymmetries/index.html> and <http://www.mhl.soton.ac.uk/public/Main/software/mPackages/UpdateInformation.html>.
[48] M. Edén, M.H. Levitt, Pulse sequence symmetries in the NMR of spinning solids. Application to heteronuclear decoupling, J. Chem. Phys. 111 (1999) 1511–1519.
[49] T. Gullion, D.B. Baker, M.S. Conradi, New, compensated Carr–Purcell sequences, J. Magn. Reson. 89 (1990) 479–484.
[50] M. Bak, J.T. Rasmussen, N.C. Nielsen, SIMPSON: a general simulation program for solid-state NMR spectroscopy, J. Magn. Reson. 147 (2000) 296–330.
[51] M. Bak, N.C. Nielsen, REPULSION: a novel approach to efficient powder averaging in solid-state NMR, J. Magn. Reson. 125 (1997) 132–139.
[52] A.E. Bennett, D.P. Weliky, R. Tycko, Quantitative conformational measurements in solid state NMR by constant-time homonuclear dipolar recoupling, J. Am. Chem. Soc. 120 (1998) 4897–4898.
[53] Y. Ishii, J.J. Balbach, R. Tycko, Measurement of dipole-coupled lineshapes in a many-spin system by constant-time two-dimensional solid state NMR with high-speed magic-angle spinning, Chem. Phys. 266 (2001) 231–236.
[54] M. Baldus, B.H. Meier, Broadband polarization transfer under magic-angle spinning: application to total through-space-correlation NMR spectroscopy, J. Magn. Reson. 128 (1997) 172–193.
[55] P. Hodgkinson, L. Emsley, The accuracy of distance measurements in solid-state NMR, J. Magn. Reson. 139 (1999) 46–59.
[56] N. Khaneja, N.C. Nielsen, Triple oscillating field technique for accurate distance measurements by solid-state NMR, J. Chem. Phys. 128 (2008) 015103.
[57] F. Vasconcelos, S. Cristol, J.F. Paul, G. Tricot, J.P. Amoureux, L. Montagne, F. Mauri, L. Delevoye, ^{17}O solid-state NMR and first-principles calculations of sodium trimetaphosphate ($Na_3P_3O_9$), tripolyphosphate ($Na_5P_3O_{10}$), and pyrophosphate ($Na_4P_2O_7$), Inorg. Chem. 47 (2008) 7327.
[58] Y.H. Tseng, Y.L. Tsai, T.W.T. Tsai, C.P. Lin, S.H. Huang, C.Y. Mou, J.C.C. Chan, Double-quantum filtered heteronuclear correlation spectroscopy under magic angle spinning, Solid State NMR 31 (2007) 55–61.